Simulations of Young Type Ia Supernova Remnants Undergoing Shock Acceleration in a Turbulent Medium

Qiyong Peng[1], Biwen Bao[1], Chuyuan Yang[2,3,4], and Li Zhang[1]

[1] Department of Astronomy, Key Laboratory of Astroparticle Physics of Yunnan Province, Yunnan University, Kunming 650091, People's Republic of China;
lizhang@ynu.edu.cn, baobiwen@ynu.edu.cn

[2] Yunnan Observatory, Chinese Academy of Sciences, Kunming,Yunnan Province 650011, People's Republic of China;

[3] Key Laboratory for the Structure and Evolution of Celestial Objects, Chinese Academy of Sciences, Kunming, People's Republic of China

[4] Center for Astronomical Mega-Science, Chinese Academy of Sciences, 20A Datun Road, Chaoyang District, Beijing 100012, People's Republic of China

Abstract

Two-dimensional cylindrical magnetohydrodynamic (MHD) simulations are implemented to investigate the dynamical properties of young type Ia supernova remnants (SNRs) undergoing shock acceleration in a turbulent medium. In our simulations, an MHD code is coupled with a semianalytical kinetic treatment of shock acceleration by means of a time-dependent effective adiabatic index. Large-scale density and magnetic field fluctuations are calculated and mapped into the computational domain before simulations. The above configurations allow us to study the time-dependent dynamical properties and magnetic field structure of a benchmark SNR undergoing shock acceleration in a turbulent medium, along with the relative positions of the contact discontinuity. Our simulation results reveal that there is a rippled forward shock, a thinner shocked ejecta layer and a denser, narrower intershock region. The resulting net effect is a higher density difference between the shocked ejecta and the shocked interstellar medium, leading to a growth of the Rayleigh–Taylor instability. The amplified magnetic field occurs not only at the contact discontinuity but also near the immediate downstream of the shock. The spatial location of the maximum magnetic field is in the vicinity of immediate downstream, which is different with Guo et al. Our derived profiles of the relative contact discontinuity positions are compatible with the results of two typical young type Ia SNRs: SN 1006 and Tycho, with the lowest value reaching $\sim$1.02 for both cases. Moreover, we find no obvious ejecta protrusions beyond the main forward shock.

Unified Astronomy Thesaurus concepts: Interstellar medium (847); Supernova remnants (1667)

1. Introduction

Galactic cosmic rays (GCRs) with energy up to a few PeV are generally believed to be accelerated inside supernova remnants (SNRs) via diffusive shock acceleration (DSA; see, e.g., Blasi 2013; Amato 2014, for recent reviews). This hypothesis is under scrutiny for a few decades, but until last few years some compelling evidence emerges owing to studying the X-ray and γ-ray emission from SNRs or nearby molecular clouds. Observed rapid X-ray variability on yearly timescales in SNR RX J1713-3946 requires extremely fast cosmic ray acceleration and quick energy losses in situ, leading to the conclusion that only synchrotron radiation of the accelerated electrons in a local amplified magnetic field can explain it reasonably when all situations are considered (Ballet 2006; Uchiyama et al. 2007). Besides, the X-ray thin rims observed in some young SNRs are also presumed to be associated with energetic electrons, and strongly amplified magnetic fields are again invoked to decipher the thicknesses of the rims (Morlino & Caprioli 2012). Recently, detections of the pion bumps in several middle-aged SNRs (IC443, W44, and W51C) provide direct evidence of efficient hadronic acceleration (Ackermann et al. 2013; Jogler & Funk 2016). Despite impressive strides made by observations, different approaches have been exploited to describe the DSA with nonlinearity and magnetic field amplification (MFA) in theory (see, e.g., Malkov & Drury 2001 for a review): kinetic semianalytical solutions, Monte Carlo numerical simulations of the full particle population, and fully numerical simulations. The semianalytical approach seems very promising for its computational convenience and adequate accuracy in terms of both particle

spectra and hydrodynamics when compared with other methods (Caprioli et al. 2010).

If the SNRs are indeed the major contributors of GCRs, then the dynamical reaction of the accelerated particles impacting on the temporal evolution of an SNR shall be contemplated. This idea is supported by observing the positions of three waves (i.e., forward shock (FS), contact discontinuity (CD), and reverse shock (RS)) in several SNRs (e.g., Warren et al. 2005; Cassam-Chenaï et al. 2007, 2008; Miceli et al. 2009; Patnaude & Fesen 2009). The observational results of the three waves' positions are in conflict with pure hydrodynamic models, indicating that a sizeable fraction of the explosion energy might be converted into GCRs. Coupling 1D self-similar simulations with a simple model of DSA (Berezhko & Ellison 1999), the modifications of hydrodynamics due to nonlinear particle acceleration is investigated (Decourchelle et al. 2000), where a thinner intershock region between the forward and RS is obtained and the hydrodynamics instabilities grow faster when efficient acceleration takes effect (see also Blondin & Ellison 2001). An updated radially symmetric model was proposed to calculate the hydrodynamic evolution of an SNR by replacing the simple DSA model with a more accurate semianalytical model (Ellison & Cassam-Chenaï 2005; Blasi et al. 2005; Ellison et al. 2007). Recently, three-dimensional hydrodynamical simulations coupled with a nonlinear diffusive shock acceleration (NLDSA) model have been exploited and the back reaction of the accelerated particles is also considered by varying the adiabatic index (Ferrand et al. 2010, 2014; Pavlović 2017), the results confirmed the previous findings regarding dynamical reaction of the accelerated particles on the

SNR morphology. Besides, the topics pertaining to SNR simulations are expanded upon in various scenarios: radiation morphologies and properties of specific SNRs (Warren & Blondin 2013; Yang et al. 2015; Zhang et al. 2017), Rayleigh–Taylor unstable interface (Jun & Norman 1996; Frashcetti et al. 2010; Wang 2011), turbulent background field and magnetic fluctuations (Balsara et al. 2001; Guo et al. 2012), interactions with preexisted stellar wind bubbles or dense clumps (Chiotellis et al. 2013; Toledo-Roy et al. 2014; Slavin et al. 2017; Wang et al. 2018), role of initial ejecta clumping and postexplosion anisotropy (Orlando et al. 2012, 2016), polarized emission properties (Schneiter et al. 2015; Bandiera & Petruk 2016; Petruk et al. 2017; Velázquez et al. 2017; Villagran et al. 2020), and mass-loading effect from embedded clouds (Pittard 2019).

Much of the previous debates revolve around the case of uniform ambient background, while there is insufficient research into this field to draw convincing conclusions concerning dynamical properties of young type Ia SNRs undergoing shock acceleration in a turbulent medium. To this end, in this paper, two-dimensional (2D) cylindrical MHD simulations of the temporal evolution of a benchmark SNR undergoing shock acceleration in a turbulent medium are performed. The DSA is described via a semianalytical model and the turbulent medium contains preexisted large-scale density and magnetic field fluctuations. We make an attempt to address how the dynamical properties and the magnetic field structure of the remnant depend on the two prior ingredients: DSA (i.e., time-dependent effective adiabatic index $\gamma_{\mathrm{eff}}(n, t)$), and a turbulent background (TB). Besides, we trace the relative positions of the contact discontinuity (referring to ratio of the forward shock radius to the contact discontinuity) which can be compared directly with X-ray observations. This paper proceeds as follow. A detailed description of our paradigm and initial setup of simulations are in Section 2. The simulation results are presented in Section 3, while some discussion and conclusions are given in Section 4.

2. Simulation Description And Initial Setup

In this section, 2D MHD cylindrical simulations of the temporal evolution for an SNR undergoing shock acceleration in a turbulent medium are delineated in details.

2.1. Modified MHD Equations

The dynamical evolution of the SNR shock wave propagating into a turbulent ambient field is simulated with the time-dependent ideal MHD equations of mass, momentum, and energy conservation:

$$\partial_t \rho + \nabla \cdot (\rho \boldsymbol{u}) = 0, \tag{1}$$

$$\partial_t \rho \boldsymbol{u} + \nabla \cdot \left(\rho \boldsymbol{u}\boldsymbol{u} - \frac{\boldsymbol{B}\boldsymbol{B}}{4\pi} \right) + \nabla P^* = 0, \tag{2}$$

$$\partial_t E + \nabla \cdot \left[(E + P^*)\boldsymbol{u} - \frac{\boldsymbol{B}(\boldsymbol{u} \cdot \boldsymbol{B})}{4\pi} \right] = 0, \tag{3}$$

and

$$\partial_t \boldsymbol{B} + \nabla \times (\boldsymbol{u} \times \boldsymbol{B}) = 0, \tag{4}$$

where ρ, $\boldsymbol{u}$, $\boldsymbol{B}$ and $P^* = P + B^2/8\pi$ are mass density, fluid velocity, magnetic field, and the total pressure (thermal pressure P plus magnetic pressure $B^2/8\pi$), respectively. E is

the total energy density,

$$E = \frac{P}{\gamma_{\mathrm{eff}}(n, t) - 1} + \frac{1}{2}\rho u^2 + \frac{B^2}{8\pi}. \tag{5}$$

In this paper, the PLUTO code developed by Mignone et al. (2007, 2012) is adopted to perform our simulations and the MHD equations are solved with a cell-centered finite-volume scheme with high-order Godunov methods. Numerical methods do not naturally preserve the condition $\nabla \cdot \boldsymbol{B} = 0$, so here a constrained transport technique is accepted to fulfill the divergence-free condition. Throughout the paper, the density is in units of m_{H} cm^{-3} and magnetic field is in units of μG. But for the cases where the turbulent medium is considered, the logarithm is taken.

2.2. Simulation Setup

The effective adiabatic index $\gamma_{\mathrm{eff}}(n, t)$ is adopted here to mimic the back reaction of accelerated particles. To calculate $\gamma_{\mathrm{eff}}(n, t)$, it is premised on the assumption that the steady solution of the NLDSA model (e.g., Blasi 2002; Amato & Blasi 2005; Caprioli et al. 2010) is applicable at each time step of the SNR evolution. The NLDSA model adopted here is semianalytical and thus is computationally very convenient. Detailed descriptions of this paradigm can be found in Caprioli et al. (2010). At each time step, the MHD code offers shock radius and velocity as inputs for the NLDSA model. The NLDSA model provides the total shock compression ratio R_{tot}, so the effective adiabatic index of the fluid to emulate the presence of accelerated particles is given by (Ellison et al. 2004)

$$\gamma_{\mathrm{eff}}(n, t) = \frac{M_s^2(R_{\mathrm{tot}} + 1) - 2R_{\mathrm{tot}}}{M_s^2(R_{\mathrm{tot}} - 1)}, \tag{6}$$

with M_s representing the sound Mach number. This is a common practice for a uniform medium (Ferrand et al. 2010; Frashcetti et al. 2010; Pavlović 2017). However, for the turbulent case considered here, each cell usually owns a different density n, a more practical manner to calculate $\gamma_{\mathrm{eff}}(n, t)$ is to utilize a derived lookup table method (see Orlando et al. 2016).

The interstellar medium (ISM) is known to be turbulent both in density and magnetic field (Lee & Jokipii 1976; Minter & Spangler 1996). Following Wang et al. (2018), we calculate the large-scale density and magnetic field fluctuations in advance and map them into the computational domain before simulations. For the fluctuating components, both the magnetic field and density are derived under the assumption of a Kolmogorov-like power spectrum, which is in accordance with the results of interstellar turbulence observations (Armstrong et al. 1995; Chepurnov & Lazarian 2010), as the form of

$$P(k) \propto \frac{1}{1 + (kL)^\Gamma}, \tag{7}$$

where the spectral index $\Gamma = 8/3$ in a 2D system and k is the magnitude of the wave vector. L stands for the coherence length of the ambient turbulence and is set to 3 pc in our simulations (Guo et al. 2012; Wang et al. 2018). The turbulence is generated by summing over a great number of discrete wave modes with random phases (Giacalone & Jokipii 1999). The random component of the magnetic field

in the cylindrical symmetry is derived by

$$\delta\boldsymbol{B}(r, z) = \sum_{n=1}^{N_m} \sqrt{C_B 2\pi k_n \Delta k_n P_B(k_n)}$$
$$\times (\sin\theta_n \hat{r} - \cos\theta_n \hat{z}) \times \exp[i(\cos\theta_n k_n r$$
$$+ \sin\theta_n k_n z + \phi_n)], \qquad (8)$$

where $P_B(k_n)$ is the power function of the wave mode with wave number k_n; θ_n is the randomly distributed propagation angle with $\cos\theta$ in the interval $(-1, 1)$ and the random phase ϕ_n satisfies $0 < \phi_n < 2\pi$. C_B is a constant that normalizes the wave amplitude and determined by $\langle \delta B^2 \rangle = B_0^2$.

The random density fluctuations follow the probability distribution below (Burlaga & Lazarus 2000; Giacalone & Jokipii 2007),

$$n(r, z) = n_0 \exp(f_0 + \delta f), \qquad (9)$$

where f_0 is a constant that determines the average density, and δf has a similar form as the magnetic field turbulent part:

$$\delta f(r, z) = \sum_{n=1}^{N_m} \sqrt{C_f 2\pi k_n \Delta k_n P_f(k_n)}$$
$$\times \exp[i(\cos\theta_n k_n r + \sin\theta_n k_n z + \phi_n)], \qquad (10)$$

where C_f as the normalization constant is determined by $\langle (\delta n)^2 \rangle = 0.4\, n_0^2$.

For simulating the SNR undergoing efficient particle acceleration in a turbulent ambient field, a series of 2D cylindrical magnetohydrodynamics simulations have been implemented here. Our simulations are set in a 2D cylindrical coordinate (r, z) with symmetry in ϕ direction as well as 2048×2048 uniform grids (Guo et al. 2012; Wang et al. 2018). A supernova shock wave is driven by injecting thermal energy and mass in a small circular region at the center of the simulation domain. The total kinetic energy and mass in the ejecta are set to $E_{sn} = 10^{51}$ erg and $M_{ej} = 1.4 M_\odot$ respectively, which are appropriate parameters for Type Ia supernova. The ambient gas number density $n_0 = 0.1$ cm^{-3}, the background temperature $T_0 = 10^4$ K. The magnetic field here includes a uniform large-scale component where $B_0 = 3\,\mu$G (along z direction), and a turbulent component δB. Detailed descriptions regarding the initial setup for the SNR blast wave can be found in Wang et al. (2018) and references therein.

3. Results

3.1. Density Distribution and Magnetic Field Structure

Figure 1 displays the density distribution at different time in a single run. For highlighting the turbulent background, the logarithm is taken. As shown in the figure, at $t = 300$ yr, the prespecified large-scale density fluctuations are evident, and the Rayleigh–Taylor instability is triggered at the contact discontinuity where the dense ejecta are decelerated by the ambient medium with a lower density (Zhou 2017a, 2017b). The finger-like structures are clearly seen in the shocked region as the shocked ejecta permeate into the shocked ISM. At later time, when the SNR expands outwards into the turbulent ISM, the ejecta become tenuous and the shocked region edged by shocked ISM and shocked ejecta becomes more prominent (i.e., intershock region). Mushroom caps occur at tips of the finger-like structures owing to the tangential velocity disparity at the interface (also known as the Kelvin–Helmholtz instability) (Jun & Norman 1996). Notably, the forward shock interacts with the turbulent background and its surface becomes

distorted, leading to shock ripples. At $t = 1000$ yr, the finger-like structures extend close to the forward shock, and the surfaces of both two shocks are severely distorted. Compared with the case without $\gamma_{eff}(n, t)$ (i.e., see middle panel of Figure 2 in Wang et al. 2018), it is apparent that the intershock region shrinks as the forward shock gets close to the contact discontinuity, owing to the lower effective adiabatic index $\gamma_{eff}(n, t)$. Notably, the shocked ejecta layer between the reverse shock and the contact discontinuity becomes thinner. The net effect is thus a higher density difference between the shocked ejecta and shocked ISM, which results in growth of the Rayleigh–Taylor instability (i.e., the finger-like structures become twisted and extend close to the forward shock).

Figure 2 shows the evolution of magnetic field structure in the same run as Figure 1. As the uniform large-scale component of background magnetic field is assumed to be along the z−axis, the MFA around the equator (tangential with respect to the shock normal) is much stronger. Different from Guo et al. (2012), the two discrete regions of MFA cannot be clearly identified in Figure 2 as the intershock region shrinks. The immediate downstream of the forward shock, where once only the background magnetic field compressed by forward shock presumed to be there, is now blended with the amplified magnetic field resulting from Rayleigh–Taylor instability. As time proceeds, the peak value of the amplified magnetic field gradually increases, indicating that the amplification has not reached a saturation. This is probably because the benchmark SNR is still in its early stage of evolution, and the maximum amplified magnetic field at $t = 1000$ yr is about 200 μG (see also Figure 3). The magnetic field inside the ejecta is low due to the outward expansion. It is worthwhile mentioning that other effects such as numerical resolution can also exert an influence on the MFA (Balsara et al. 2001; Guo et al. 2012).

More specifically, the output data of our simulations at $t = 1000$ yr are analyzed and the results are depicted in Figure 3. At the top left panel, owing to turbulent ambient medium, the shock position varies with the angle between the shock radius and the r−axis (from minimum $\sim$6.53 pc to maximum $\sim$6.93 pc). Regarding the averaged shock position ($\sim$6.72 pc), those variations across the forward shock correspond to a relative small percentage from $\sim$−2.8% to $\sim$+3.1%. It is noteworthy that the actual variations of the shock position heavily depend on the specific structure of the turbulent medium. When part of the forward shock encounters the turbulent ambient medium with a relatively high density, it will suffer more suppression. The net effect of the forward shock interacting with the turbulent background is the appearance of a corrugated surface. In the top right panel, it is clear to see that the MFA occurs in the intershock region (not only near the Rayleigh–Taylor unstable region, but also in the vicinity of immediate shock downstream). Moreover, the radially averaged magnetic field strength reaches a maximum value of about 23 μG. It should be pointed out that when our data are postprocessed for the radially averaged magnetic field, a larger (close to the remnant outer rim) radius may count some grid cells with ambient magnetic field as the whole shock surface is distorted.

The bottom left panel of Figure 3 illustrates the time evolution of the maximum magnetic field strength and its relative location as an indicator of MFA in downstream. Here, the relative location refers to the ratio between the radius of the cell where the maximum magnetic field strength stores and the
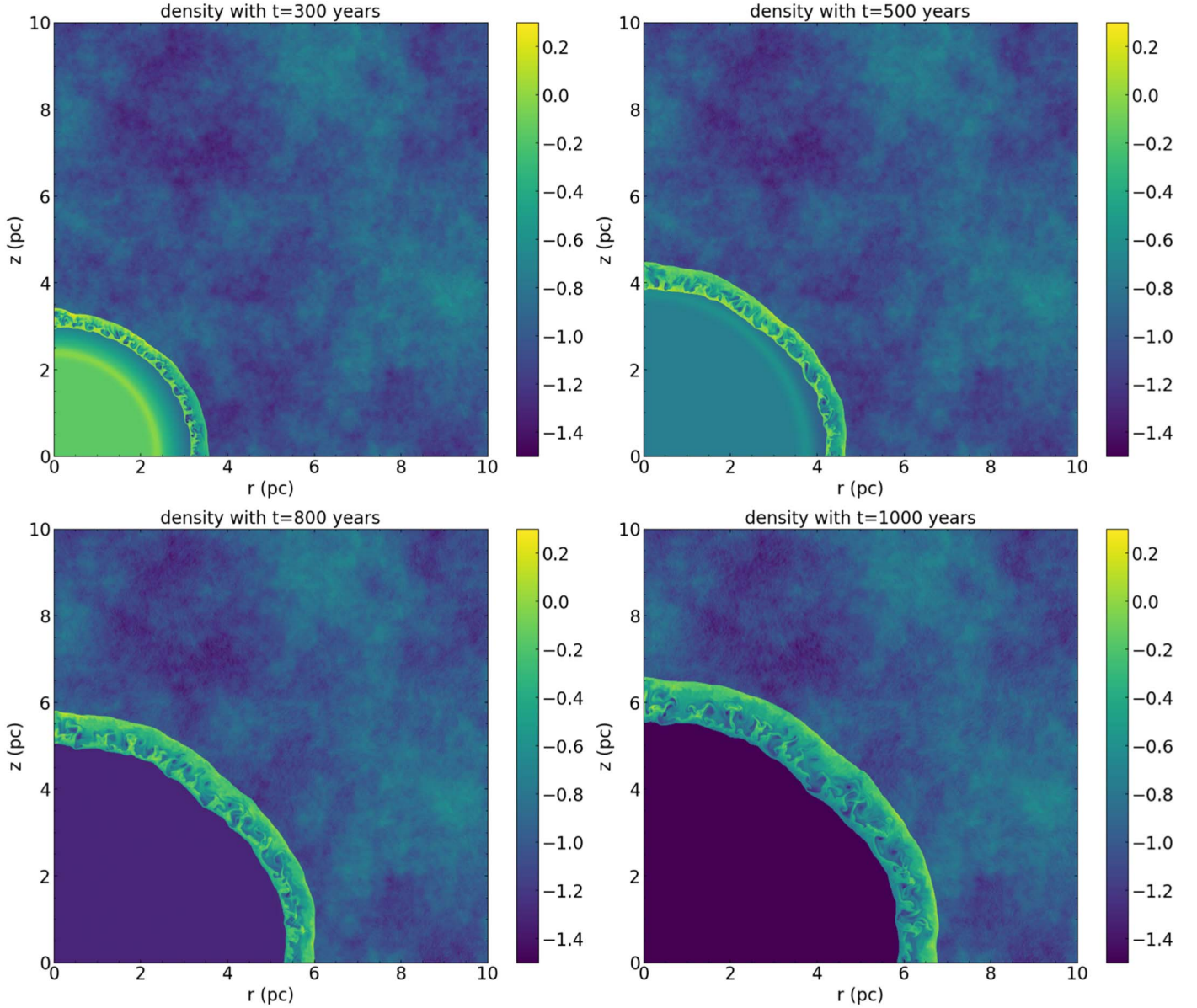
Figure 1. Density distributions in one run at different times. The color bar shows the logarithm of density in units of m_H cm^{-3}.

radius of the forward shock just ahead of it (especially important for the cases where the forward shock becomes distorted) and we begin our tracing when the shock structure and Rayleigh–Taylor fingers have clearly formed. It can be seen from the plot that the maximum magnetic field increases to about 200 μG within 1000 yr (the corresponding $\gamma_{\rm eff} \sim 1.29$), which is much larger than what is expected from the simple shock compression. Guo et al. (2012) pointed out that the spatial location of the maximum magnetic field is typically not near the immediate downstream region by detailed analysis. However, as shown in the bottom left panel of Figure 3, it is evident to see that the spatial location of the maximum magnetic field is quite near the shock front for most time. It is not surprising to see the discrepancy between our results and the results given by Guo et al. (2012), as the discrepancy could be mainly attributed to the time-dependent effective adiabatic index $\gamma_{\rm eff}(n, t)$ adopted here. For a lower $\gamma_{\rm eff}(n, t)$, the shocked region shrinks meanwhile the Rayleigh–Taylor unstable structures extend close to the forward shock.

As a consequence, the two distinct regions of MFA seen in Guo et al. (2012) now merge almost as one region (difficult to disentangle one from the other) and the spatial location of maximum magnetic field could be in the vicinity of immediate shock downstream region. The bottom right panel of Figure 3 illustrates the statistical histograms of the amplified magnetic field distribution at $t = 1000$ yr, which can also be an indicator of the effect of MFA. As shown in the plot, the magnetic field can be amplified substantially in quite a few cells with values larger than those from simple shock compression. When interpreting the observed X-ray thin rims and their properties in some SNRs, a local amplified magnetic field at or in the proximity of the downstream shock is often suggested. With our simulation, it is completely possible to reproduce such a feature and in fact the spatial location of radially averaged amplified magnetic field could even get closer to the forward shock as the data-processing routines in our code may count some cells with ambient magnetic field at the outmost part of the remnant.
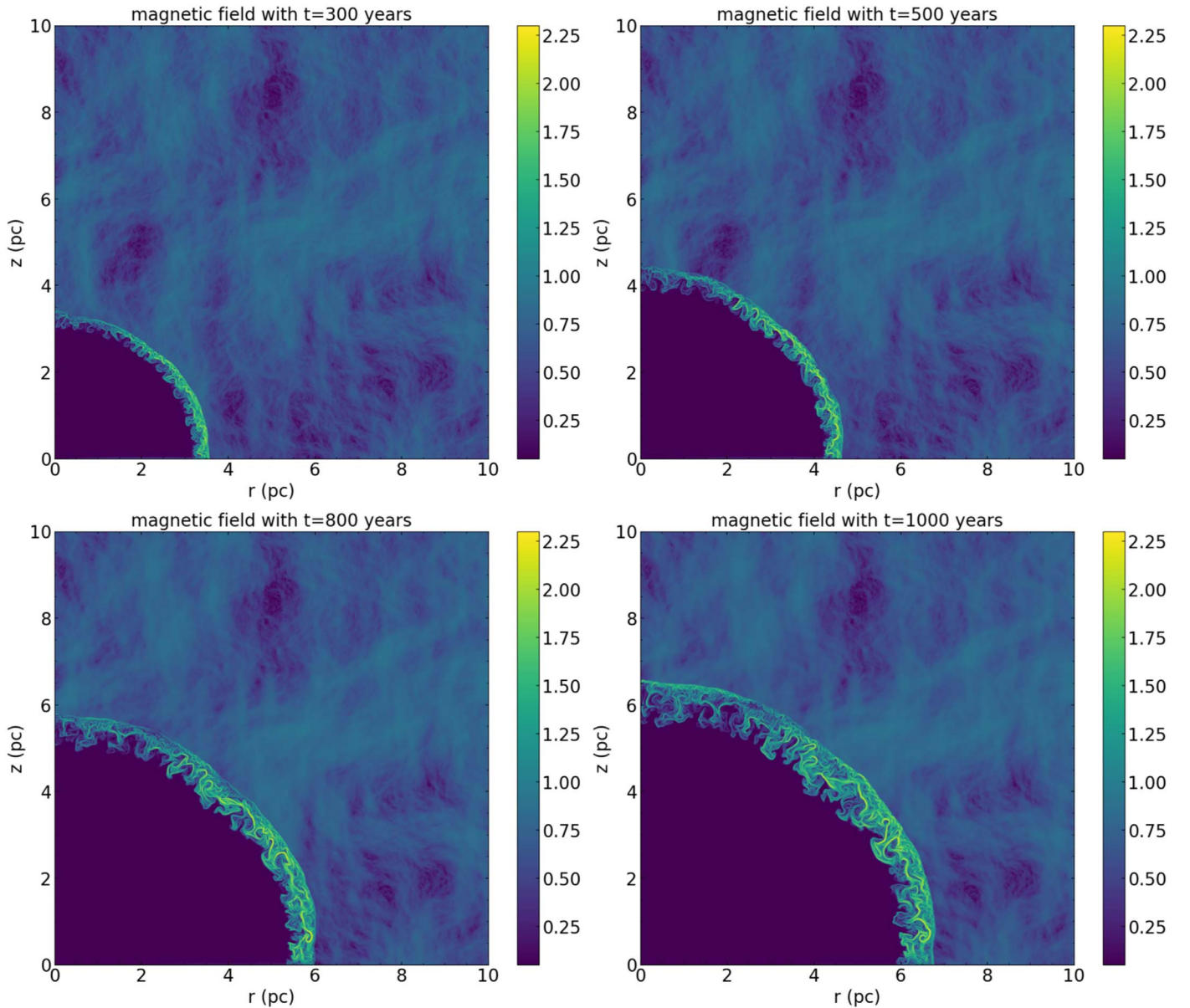
Figure 2. Structures of the magnetic field in one run at different times. The color bar shows the logarithm of magnetic field in units of μG.

3.2. Relative Positions of Contact Discontinuity

The relative positions of contact discontinuity, which we define as the ratio of the forward shock radius to the contact discontinuity, can be a practicable tracer probing efficient shock acceleration at SNRs according to previous works (Decourchelle et al. 2000; Blondin & Ellison 2001).

In Figure 4, we compare our derived profiles with the X-ray observational results for two typical young Type Ia SNRs: SN 1006 (Miceli et al. 2009) and Tycho (Warren et al. 2005). The solid lines in the plots represent our derived profiles while the shaded area marks the results derived from X-ray observations. For SN 1006 and Tycho, we make use of the profiles at $t = 1000$ yr and $t = 430$ yr, respectively. As illustrated in Figure 4, our derived profiles are well compatible with the observational results for both two SNRs. Regarding SN 1006, the relative positions of contact discontinuity are limited to within the range of ~ 1.0–1.15 from the combined analysis of H_α image as well as X-ray ejecta emission (Miceli et al. 2009)

while our derived profile is between ~ 1.02 and 1.16. Such an agreement also applies for the case of Tycho, where the our result spans from ~ 1.02 up to ~ 1.13.

It should be noted that the lowest value of our derived profile in both cases is about 1.02. However, most X-ray observations have suggested ~ 1.0 as the lowest value for both cases, which may indicate that the Rayleigh–Taylor fingers are extremely close to or even overtaking the forward shock (Warren et al. 2005; Cassam-Chenaï et al. 2007, 2008). Moreover, we found no evident ejecta protruding beyond the main forward shock. Such protrusions have been identified by several authors both in Tycho and SN 1006 (Velázquez et al. 1998; Rakowski et al. 2011) despite the fact that their actual origin is still in debate: ejecta clumping imposed as initial conditions, hydrodynamic instabilities developing at the surface of contact discontinuity, or preexisting inhomogeneous ambient structures (Wang & Chevalier 2001; Orlando et al. 2012; Warren & Blondin 2013; Williams et al. 2017; Sato et al. 2019). The mentioned inconsistency may imply that there is some room for other
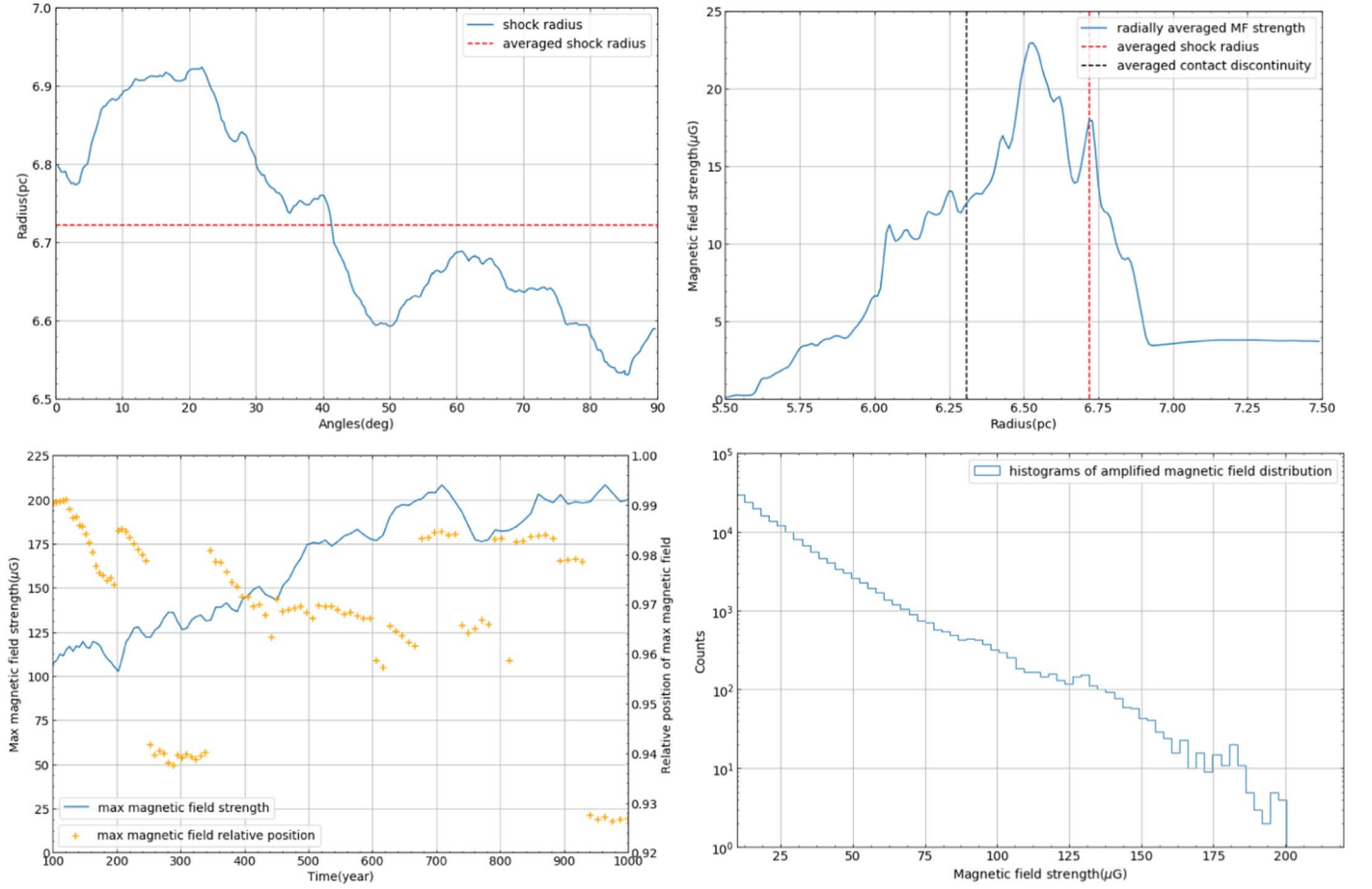
Figure 3. Top left: the solid line represents shock position at different angles (with regard to *r*-axis), while the dotted line shows the angularly averaged shock position. Top right: radially averaged magnitude of the magnetic field from the 2D simulations in units of μG. The red dotted line represents the angularly averaged shock position, while black dotted line stands for the angularly averaged position of the contact discontinuity. Bottom left: time evolution of the maximum magnetic field strength and its location relative to the shock front: the blue solid line depicts the maximum magnetic field strength, while the orange solid line represents the relative location of the maximum magnetic field strength. Bottom right: the statistical histograms of the amplified magnetic field distribution.

scenarios which can further enhance the growth of Rayleigh–Taylor instability or even modify the initial ejecta structures, thus reducing the relative positions of contact discontinuity.

3.3. A Compared Inspection

What we have concluded in previous sections from our simulation results should deserve a compared inspection with the case of no acceleration. To accomplish it, our data are analyzed and the results are displayed in Figures 5 and 6, respectively.

In Figure 5, we present the same contents as in Figure 3, except we add the results of the case with no efficient acceleration. A few comments regarding the results are given as follows.

Considering the turbulent background solely, the forward shock front extends for about 0.6 pc and retains ripples. The shock position varies from minimum ~7.15 pc to maximum ~7.48 pc. Regarding the averaged shock position (~7.34 pc), those variations across the forward shock correspond to a even smaller percentage (~−2.6% to ~+1.9%) than the case with efficient acceleration. This discrepancy may reveal that the inclusion of $\gamma_{\mathrm{eff}}(n, t)$ leads to an aggravation of the shock ripples which is essentially due to ambient turbulence. As for the radially averaged magnetic field, its maximum value reaches about 12 μG at the intershock region which is much

smaller than the case with efficient acceleration by a factor of about 1.9. The shrink of the intershock region can also be clearly seen by viewing the distance between the averaged forward shock radius and the averaged contact discontinuity, where the averaged forward shock shrinks while the latter roughly stays the same.

Similar to the radially averaged magnetic field profile, time evolution of the maximum magnetic field strength could also be an indicator of MFA. The bottom left panel in Figure 5 depicts the time evolutions of the maximum magnetic field strength and its relative locations in two different situations. In both two cases, it seems that the maximum magnetic field strength increases with time and has not reached a saturation as it is still in the early stage of the evolution. When $\gamma_{\mathrm{eff}}(n, t)$ is considered, the maximum magnetic field strength substantially enhances as time proceeds and is much larger than the case with no efficient acceleration. The bottom right panel illustrates the statistical histograms of the amplified magnetic field distribution. As shown in the plot, the magnetic field can be amplified substantially in quite a few cells with values larger expected from simple jump condition in both cases while the inclusion of $\gamma_{\mathrm{eff}}(n, t)$ brings about a stronger amplification.

As for the relative location of the maximum magnetic field strength, it merits a detailed interpretation. Considering the ambient turbulent background solely, the relative location
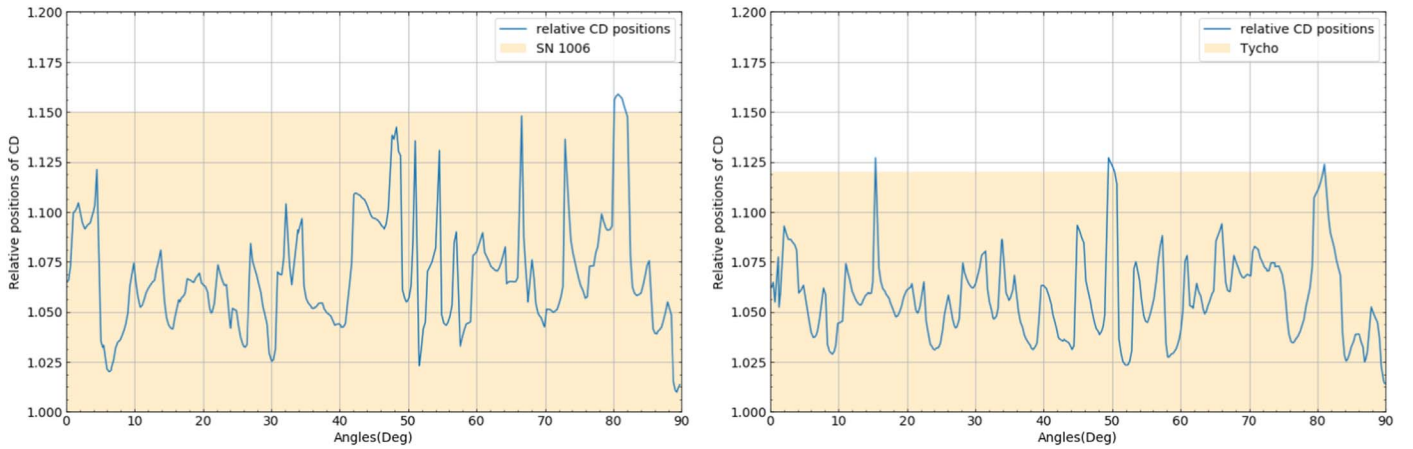
Figure 4. Relative positions of contact discontinuity (ratio of the forward shock radius to the contact discontinuity). The shaded area marks the results derived from X-ray observations of SN 1006 (Miceli et al. 2009) and Tycho (Warren et al. 2005), respectively.

varies with time which implies there may exist some small regions with amplified magnetic field comparable with each other. These small regions are distributed randomly in the shocked region and most of them are near contact discontinuity. In fact, such changes can be viewed as competition between the two regions of MFA (Guo et al. 2012). The amplification in the immediate downstream region is principally due to vortical flow produced at rippled shock front, which can distort and stretch the magnetic field lines, thus resulting in a strong amplification. The other region is closely associated with the Rayleigh–Taylor instability at the contact discontinuity. Once $\gamma_{eff}(n, t)$ is considered, the two regions seem to merge while the relative location shifts to the vicinity of immediate downstream. It is obvious that the spatial location of maximum magnetic field strength is quite near immediate downstream region for most time which reveals that amplified magnetic field could occur in the immediate vicinity of an SNR shock.

Figure 6 illustrates the comparison of our derived profiles with the X-ray observational results for two typical young Type Ia SNRs: SN 1006 (Miceli et al. 2009) and Tycho (Warren et al. 2005). As is clearly depicted, the derived profiles are well compatible with the observational results for both two SNRs only in context of efficient acceleration where $\gamma_{eff}(n, t)$ is at work. Instead, the derived profiles of the case with no efficient acceleration exhibit some deviations from the observational results.

4. Discussion and Conclusions

Based on a series of 2D cylindrical MHD simulations, the evolution of a benchmark SNR undergoing efficient shock acceleration in a turbulent medium has been investigated in this paper. A common trait of many previous works is the use of idealized uniform ambient background while the interstellar medium is known to be turbulent both in density and magnetic field (Lee & Jokipii 1976; Minter & Spangler 1996). Here, we choose a turbulent description of the ambient medium where its fluctuating component is derived under the assumption of a Kolmogorov-like power spectrum. Coupling our simulations with a realistic semianalytical acceleration model is reasonable, given that it is widely believed that galactic cosmic rays are produced in SNRs via DSA. The presence of accelerated particles and their back reaction on the SNR morphology could

be mimicked by a time-dependent effective adiabatic index $\gamma_{eff}(n, t)$.

Initially, when both conditions ($\gamma_{eff}(n, t)$ and turbulent background) are satisfied, a narrower, denser intershock region and a thinner shocked ejecta layer are obtained. The resulting net effect is a higher density difference between the shocked ejecta and the shocked ISM, leading to a rapid growth of the Rayleigh–Taylor instability. Rippled forward shock and distorted reverse shock are clearly seen in the density profiles. The two MFA regions identified in Guo et al. (2012) now almost merge because of the shrunken intershock region as well as the growth of the Rayleigh–Taylor instability, resulting in the occurrence of strongly amplified magnetic field near the immediate downstream. More explicitly, the fundamental cause of such amplification is two-fold: partly due to a contribution from vortical flow and partly associated with the enhanced Rayleigh–Taylor instability. The spatial location of the maximum magnetic field is quite near the immediate downstream, indicating that amplified magnetic field could occur in the immediate vicinity of an SNR shock. It is not surprising to see the discrepancy between our results and the results given by Guo et al. (2012), which could be attributed to the time-dependent effective adiabatic index $\gamma_{eff}(n, t)$ adopted here. Reproducing such a feature is pivotal, as X-ray thin rims seen in some SNRs, and their coincidence with the inferred shock locations have suggested an amplified magnetic field occurring at or within a short distance to forward shock. The maximum values of density and magnetic field are also obtained under this circumstance.

Besides, we also trace the relative positions of contact discontinuity and the derived profiles are consistent with the observational results for two typical Ia SNRs: SN 1006 and Tycho. It is noteworthy that the lowest value of our derived profile in both cases is about 1.02 which seems at odds with suggested value ~1.0 from X-ray observations (Warren et al. 2005; Cassam-Chenaï et al. 2007, 2008; Miceli et al. 2009). Meanwhile, we also find no obvious ejecta protrusions which have been identified by several authors both in Tycho and SN 1006 irrespective of their elusive origin (Velázquez et al. 1998; Rakowski et al. 2011). The foregoing inconsistency indicates us that there may exist alternative scenarios which can further enhance Rayleigh–Taylor instability or even modify the initial ejecta profile, thus reducing the relative positions of contact discontinuity to match observations. As a recent attempt,
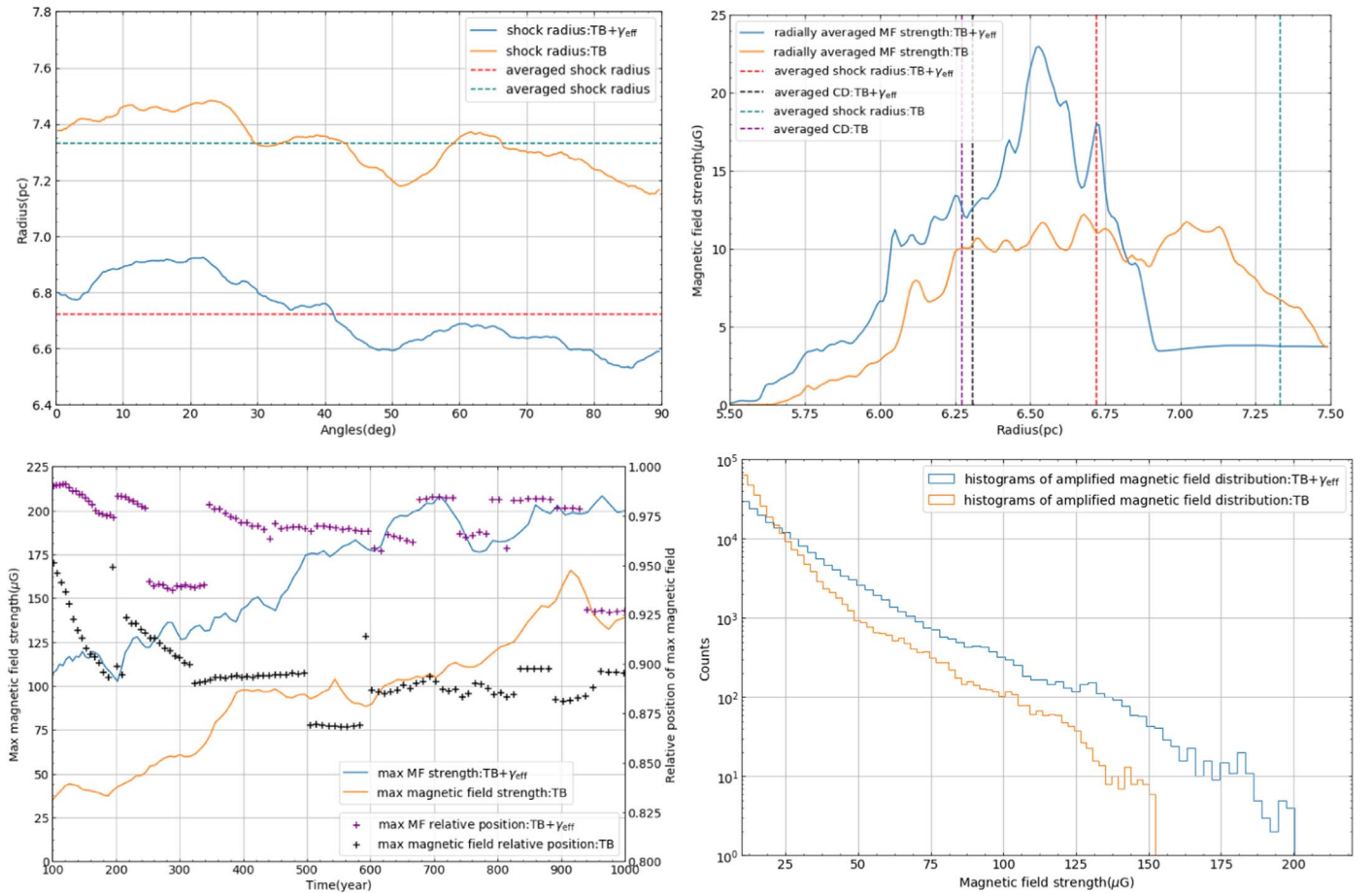
Figure 5. Top left: the solid lines represent shock position at different angles (with regard to r−axis), while the dotted lines show the angularly averaged shock position. Top right: radially averaged magnitude of the magnetic field in units of μG. The dotted lines represent the angularly averaged shock position, as well as the angularly averaged position of the contact discontinuity. Bottom left: time evolution of the maximum magnetic field strength and its location relative to the shock front: the solid lines depict the maximum magnetic field strength, while the dotted lines represent the relative location of the maximum magnetic field strength. Bottom right: the statistical histograms of the amplified magnetic field distributions.

Ferrand et al. (2019) have investigated the imprint of an asymmetrical SN Ia explosion on the resulting SNR morphology with a state-of-the-art scheme. The clumpy patterns are clearly seen in their synthetic thermal emission maps and the entire SNR morphology seems very realistic-looking (resembling the X-ray observational results of Tycho). Some Rayleigh–Taylor fingers are even protruding beyond the main forward shock, which is in accord with the findings in Orlando et al. (2012) where the ejecta clumping serves as an underlying assumption.

Moreover, by postprocessing our data, a compared inspection with the case of no acceleration is given. The shock positions, radially averaged magnetic fields, time evolutions of the maximum magnetic field strength, and its relative locations in different circumstances have been depicted. The closer analysis reveals that when consider the turbulent background solely, the forward shock extends but the ripples seem to be less obvious. The maximum radially averaged magnetic field is smaller than the case with efficient acceleration by a factor of about 1.9. Similar conclusion can be drawn for the evolution of the maximum magnetic field strength. As for the relative location of the maximum magnetic field strength, it varies with time and is not in the vicinity of immediate downstream for most time, which is consistent with Guo et al. (2012). One limitation of our study is the adoption of a same initial setup for

both SN 1006 and Tycho, while the actual interstellar medium structures surrounding them could be different due to their separate Galactic latitudes. Moreover, the actual interstellar medium structure might be much more complicated than the simple scenario proposed here for both cases (Reynoso et al. 2013; Williams et al. 2013).

One of the major problems that the SNR–CR paradigm encounters is whether the shock acceleration could accelerate particles to PeV in its nonlinear version. One promising answer lies in the MFA which could boost the maximum energy of the particles. However, it is worth recalling that the maximum energy can be achieved only if the amplification occurs both upstream and downstream of the shock (mainly affected by the value of the amplified magnetic field upstream). If the particles cannot be scattered back to the shock effectively, the acceleration processes would be inefficient and the particles could escape the system either from one side or the other (Morlino 2017). In our simulations, shocked plasma in downstream is usually highly turbulent and Rayleigh–Taylor instability could amplify the local magnetic field, converting a fraction of the turbulent motion into magnetic energy (Giacalone & Jokipii 2007). So it is prone to achieving a magnetic amplification downstream in the simulations while the triggering mechanism in the upstream has not yet been fully understood (Caprioli et al. 2018). Recent X-ray observations of
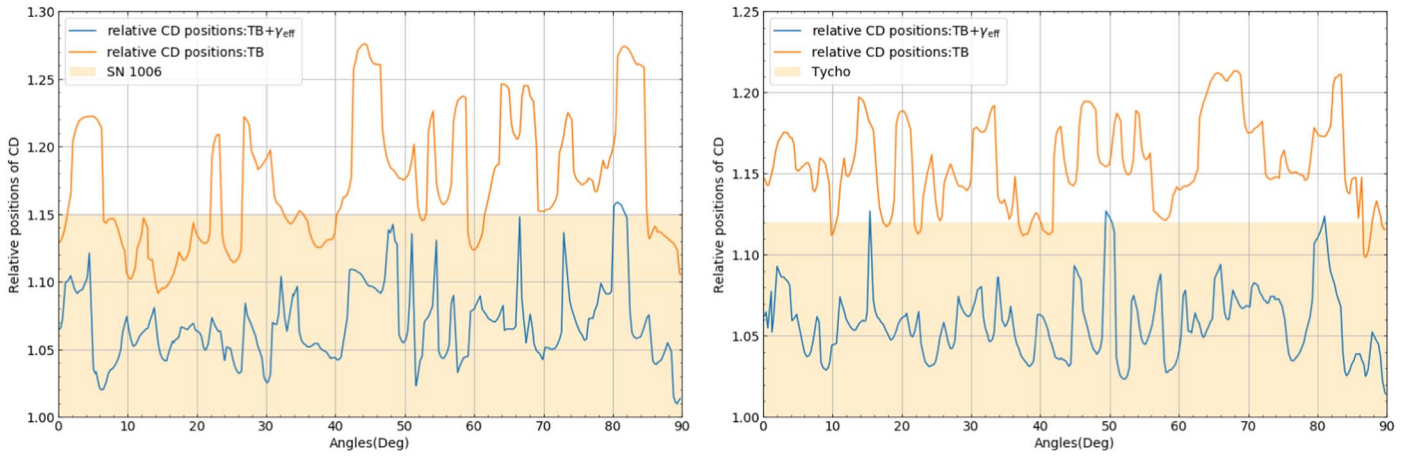
Figure 6. Relative positions of contact discontinuity (ratio of the forward shock radius to the contact discontinuity). The shaded area marks the results derived from X-ray observations of SN 1006 (Miceli et al. 2009) and Tycho (Warren et al. 2005), respectively.

SNR shocks also reveal substantial evidence that MFA occurs upstream, which in turn calls for efforts to look for a reliable solution to trigger amplification in upstream.

Software: PLUTO (Mignone et al. 2007, 2012), Jupyter Notebook,[5] Numpy (van der Walt et al. 2011), Pandas (McKinney 2010), Matplotlib (Hunter 2007).

ORCID iDs

Chuyuan Yang ⬤ https://orcid.org/0000-0001-6903-5306
Li Zhang ⬤ https://orcid.org/0000-0002-7824-4289

References

Ackermann, M., Ajello, M., Albert, A., et al. 2013, Sci, 339, 807
Amato, E. 2014, IJMPD, 23, 1430013
Amato, E., & Blasi, P. 2005, MNRAS Lett, 364, 76
Armstrong, J. W., Rickett, B. J., & Spangler, S. R. 1995, ApJ, 443, 209
Ballet, J. 2006, AdSpR, 37, 1902
Balsara, D., Benjamin, R. A., & Cox, D. P. 2001, ApJ, 563, 800
Bandiera, R., & Petruk, O. 2016, MNRAS, 459, 178
Berezhko, E. G., & Ellison, D. C. 1999, ApJ, 526, 385
Blasi, P. 2002, APh, 16, 429
Blasi, P. 2013, A&ARv, 21, 70
Blasi, P., Gabici, S., & Vannoni, G. 2005, MNRAS, 361, 907
Blondin, J. M., & Ellison, D. C. 2001, ApJ, 560, 244
Burlaga, L. F., & Lazarus, A. J. 2000, JGR, 105, 2357
Caprioli, D., Amato, E., & Blasi, P. 2010, APh, 33, 307
Caprioli, D., Kang, H., Vladimirov, A. E., & Jones, T. W. 2010, MNRAS, 407, 1773
Caprioli, D., Zhang, H., & Spitkovsky, A. 2018, JPlPh, 84, 715840301
Cassam-Chenaï, G., Hughes, J. P., Ballet, J., & Decourchelle, A. 2007, ApJ, 665, 315
Cassam-Chenaï, G., Hughes, J. P., Reynoso, E. M., Badenes, C., & Moffett, D. 2008, ApJ, 680, 1180
Chepurnov, A., & Lazarian, A. 2010, ApJ, 710, 853
Chiotellis, A., Kosenko, D., Schure, K. M., Vink, J., & Kaastra, J. S. 2013, MNRAS, 435, 1659
Decourchelle, A., Ellison, D. C., & Ballet, J. 2000, ApJL, 543, L57
Ellison, D. C., & Cassam-Chenaï, G. 2005, ApJ, 632, 920
Ellison, D. C., Decourchelle, A., & Ballet, J. 2004, A&A, 413, 189
Ellison, D. C., Patnaude, D. J., Slane, P., Blasi, P., & Gabici, S. 2007, ApJ, 661, 879
Ferrand, G., Decourchelle, A., Ballet, J., Teyssier, R., & Frashcetti, F. 2010, A&A, 509, L10
Ferrand, G., Decourchelle, A., & Safi-Harb, S. 2014, ApJ, 789, 49
Ferrand, G., Warren, D. C., Ono, M., et al. 2019, ApJ, 877, 136
Frashcetti, F., Teyssier, R., Ballte, J., & Decourchelle, A. 2010, A&A, 515, A104
Giacalone, J., & Jokipii, J. R. 1999, ApJ, 520, 204
Giacalone, J., & Jokipii, J. R. 2007, ApJL, 663, L41
Guo, F., Li, S., Li, H., et al. 2012, ApJ, 747, 98
Hunter, J. D. 2007, CSE, 9, 90
Jogler, T., & Funk, S. 2016, ApJ, 816, 100
Jun, B.-I., & Norman, M. L. 1996, ApJ, 465, 800
Korolev, V. V., Vasiliev, E. O., Kovalemko, I. G., & Shchekinov, Y. A. 2015, ARep, 59, 690
Lee, L. C., & Jokipii, J. R. 1976, ApJ, 206, 735
Malkov, M. A., & Drury, L. 2001, RPPh, 64, 429
McKinney, W. 2010, in Proc. 9th Python in Science Conf. 445, Data Structures for Statistical Computing in Python, ed. S. van der Walt & J. Millman (Trieste: SISSA), 51
Miceli, M., Bocchino, F., Lakubovskyi, D., et al. 2009, A&A, 501, 239
Mignone, A., Bodo, G., Massaglia, S., et al. 2007, ApJS, 170, 228
Mignone, A., Zanni, C., Tzeferacos, P., et al. 2012, ApJS, 198, 7
Minter, A. H., & Spangler, S. R. 1996, ApJ, 458, 194
Morlino, G. 2017, in IAU Symp. 331, Supernova 1987A:30 years later - Cosmic Rays and Nuclei from Supernovae and their aftermaths (Cambridge: Cambridge Univ. Press), 230
Morlino, G., & Caprioli, D. 2012, AIPC, 1505, 241
Orlando, S., Bocchino, F., Miceli, M., Petruk, O., & Pumo, M. L. 2012, ApJ, 749, 156
Orlando, S., Miceli, M., Pumo, M. L., & Bocchino, F. 2016, ApJ, 822, 22
Patnaude, D. J., & Fesen, R. A. 2009, ApJ, 697, 535
Pavlović, M. Z. 2017, MNRAS, 468, 1616
Petruk, O., Bandiera, R., Beshley, V., et al. 2017, MNRAS, 470, 1156
Pittard, J. M. 2019, MNRAS, 488, 3376
Rakowski, C. E., Laming, J. M., Hwang, U., et al. 2011, ApJL, 735, L21
Reynoso, E. M., Hughes, J. P., Moffett, D., et al. 2013, ApJ, 145, 104
Sato, T., Hughes, J. P., Williams, B. J., et al. 2019, ApJ, 879, 64
Schneiter, E. M., Velázquez, P. F., Reynoso, E. M., et al. 2015, MNRAS, 449, 88
Slavin, J. D., Smith, R. K., Foster, A., et al. 2017, ApJ, 846, 77S
Toledo-Roy, J. C., Velázquez, P. F., Esquivel, A., & Giacani, E. 2014, MNRAS, 442, 229
Uchiyama, Y., Aharonian, F., Tanaka, T., Takahashi, T., & Maeda, Y. 2007, Natur, 449, 576
van der Walt, S., Colbert, S. C., & Varoquaux, G. 2011, CSE, 13, 22
Velázquez, P. F., Gomez, D. O., Dubner, G. M., et al. 1998, A&A, 334, 1060
Velázquez, P. F., Schneiter, E. M., Reynoso, E. M., et al. 2017, MNRAS, 466, 4851
Villagran, M. A., Velázquez, P. F., Gomez, D. O., et al. 2020, MNRAS, 491, 2855

---

[5] https://jupyter.org/

Wang, C. Y. 2011, MNRAS, 415, 83
Wang, C. Y., & Chevalier, R. A. 2001, ApJ, 549, 1119
Wang, Y. Y., Bao, B. W., Yang, C. Y., & Zhang, L. 2018, MNRAS, 478, 2948
Warren, D. C., & Blondin, J. M. 2013, MNRAS, 429, 3099
Warren, J. S., Hughes, J. P., Badenes, C., Ghavamian, P., et al. 2005, ApJ, 634, 376
Williams, B. J., Borkowski, K. J., Ghavamian, P., et al. 2013, ApJ, 770, 129

Williams, B. J., Coyle, N. M., Yamaguchi, H., et al. 2017, ApJ, 842, 28
Yang, C. Y., & Liu, S. M. 2013, ApJ, 773, 138
Yang, C. Y., Liu, S. M., Fang, J., & Li, H. 2015, A&A, 573, A37
Zhang, M. F., Tian, W. W., Leahy, D. A., et al. 2017, ApJ, 849, 147
Zhou, Y. 2017a, PhR, 720, 1
Zhou, Y. 2017b, PhR, 723, 1